Electronic Supporting Information

Integration of Functionalized Graphene Nano-Network into Planar Perovskite Absorber for High Efficiency Large Area Solar Cells

Yong Wang[a], Yuanyuan Zhou[b], Taiyang Zhang[a], Ming-Gang Ju[c], Lin Zhang[b], Miao Kan[a], Yihui Li[a], Xiao Cheng Zeng[c], Nitin. P. Padture[b], Yixin Zhao[a]*

a. School of Environmental Science and Engineering, Shanghai Jiao Tong University, 800 Dongchuan Road, Shanghai 200240, China

b. School of Engineering, Brown University, Providence, Rhode Island 02912, United States

c. Department of Chemistry, University of Nebraska-Lincoln, Lincoln, Nebraska 68588, United States

E-mail: yixin.zhao@sjtu.edu.cn

Experimental Section

Materials.

Amino-functionalized graphene (G-NH_2) was synthesized using a procedure described elsewhere[1-2]. MAI were synthesized according to our previously reported technique. PbI_2 were purchased from Alfa Aesar. Anhydrous dimethylformamide (DMF) and dimethyl sulfoxide (DMSO) were purchased from Sigma-Aldrich. The SnO_2 colloid precursor was obtained from Alfa Aesar (tin(IV) oxide, 15% in H_2O colloidal dispersion).

Solar Cell Fabrication.

The solar cells were fabricated on FTO substrates (TEC 15). The substrates were washed sequentially with detergent (2% Hellmanex in water), deionized water, ethyl alcohol, isopropanol, and finally cleaned under UV-ozone treatment for 10 min. The patterned TEC-15 FTO substrate was coated with a compact TiO_2 layer by spray pyrolysis of 0.2M Ti(IV) bis (ethyl acetoacetate)-diisopropoxide in 1-butanol solution at 450 °C, followed by annealing at 450 °C for one hour. The SnO_2 colloid precursor (1.5% in H_2O colloidal dispersion) was then spin-coated onto c-TiO_2/FTO substrates at 3000 rpm for 30 s, followed by baking on a hot plate in ambient air at 180 °C for 30 min.

The precursor solution was prepared by dissolving MAI (1.4 M), PbI_2 (1.4 M) in DMF: DMSO with 4:1 (v/v) ratio to make a clear $MAPbI_3$ solution. In order to incorporate different amounts of G-NH_2 in the $MAPbI_3$ precursor solution, 0.05, 0.10, and 0.20 mg·mL^{-1} of G-NH_2 were dispersed in the solvent (anhydrous DMF: DMSO 4:1 (v/v)) using 2-h sonication prior to making the perovskite solution (i.e., $MAPbI_3$/G-NH_2, $MAPbI_3$/0.1G-NH_2, $MAPbI_3$/0.2G-NH_2), respectively. For comparison, we also incorporated 0.05 mg·mL^{-1} rGO in the $MAPbI_3$ precursor solution. All other steps in device preparation were exactly the same. The perovskite layers were deposited in a

dry glovebox by spin-coating the as-prepared precursor solutions onto the SnO_2/c-TiO_2/FTO substrates at 5000 rpm for 20 s, with an accelerating rate of 5000 rpm·s^{-1}. 500 uL chlorobenzene was dripped onto the spinning substrate 15 s before the end of the spin-coating program. The perovskite film acquired was then annealed at 100 °C for 20 min.

A layer of hole transport material (HTM) was spin-coated on top of the annealed films, which consisted of 0.1 M spiro-MeOTAD, 0.035 M bis(trifluoromethane) sulfonamide lithium salt (Li-TFSi), and 0.12 M 4-tert-butylpyridine (tBP) in chlorobenzene/acetonitrile (10:1, v/v) solution at 4000 rpm for 25 s. Finally, a 100-nm thick Ag layer was deposited by thermal evaporation.

Characterization

The crystal structures of the formed perovskite films were characterized using XRD (Shimadzu XRD-6100 diffractometer with Cu Kα radiation). The absorption spectra of the thin films were measured on an Cary-60 UV-vis spectrophotometer. FTIR experiments were conducted on a Tensor 27 FTIR spectrometer (Nicolet 6700), using KBr pellets of the solid samples. The perovskite films were characterized using a SEM (JEOL JSM-7800F Prime). High-resolution characterization was performed using a TEM (JEOL 2100F), operated at 200 kV accelerating voltage, equipped with an EDS (Oxford Instruments). Thin films for TEM studies were prepared using the same procedure as above, but were deposited directly onto the TEM grids (SPI). The TRPL was recorded on a PTI QM/TM/IM fluorescence spectrofluorometer. c-AFM tip (Pt/Ir coated Si; Budget Sensor ContE-G; force constant = 0.2 N/m; radius ~20 nm; resonance frequency ~14 kHz) was used to scan the sample surface in the contact mode and the current was measured when the probe encountered conducting locations. The image of local variations of current (typically in pA to nA range) is recorded simultaneously with the sample topography and presented as a current map. The small force constant of the c-AFM cantilever helps to image soft surfaces

without deformation. The conducting probe contacts the perovskite films and measures the current distribution on the surface under a fixed bias. The c-AFM images were recorded at 1 V DC bias.

The J-V characteristics were measured with a Keithley 2401 source meter with a scan rate of 0.05 $V \cdot s^{-1}$ under the simulated AM 1.5G illumination (100 $mW \cdot cm^{-2}$) using Enlitech's 3A light source. The EQE was measured on a QE-3011 system (Enlitech). The TPC/TPV were generated by a microsecond pulse of a white light incident on solar cells under short circuit conditions (by a very low resistor at 20 Ω) and open circuit condition (by a large resistor at 1 MΩ). No background light was applied. IMPS was measured to compare the electron transport dynamic in the PSCs. The electron transit time (τd) in PSCs can be obtained by $\tau_d = 1/2\pi f_{IMPS}$, where f_{IMPS} is the frequency of the minimum imaginary component in IMPS measurements. These measurements were performed under white light.

Computational Methods

All first-principles computations are performed based on density-functional theory (DFT) methods as implemented in the Vienna ab initio simulation package (VASP 5.4). An energy cutoff of 520 eV is used, and the atomic positions are optimized using the conjugate gradient scheme without any symmetric restrictions, until the maximum force on each atom is less than 0.02 eV. Å-1. The charge densities are computed using the Perdew-Burke-Ernzerhof (PBE) functional, and the ion cores are described by using the projector augmented wave (PAW) method. Grimme's DFT-D3 correction is adopted to describe the long-range van der Waals interaction. A 2×2×1 k-point grid is used for the $MAPbI_3$/G-NH_2 and the $MAPbI_3$/rGO slabs. The difference of charge density (eg. $\Delta\rho=\rho_{MAPbI3/G\text{-}NH2}-\rho_{MAPbI3}-\rho_{G\text{-}NH2}$, $\rho_{MAPbI3/G\text{-}NH2}$, ρ_{MAPbI3} and $\rho_{G\text{-}NH2}$ are charge densities of $MAPbI_3$/G-NH_2, $MAPbI_3$ and G-NH_2, respectively) between the whole supercell and the sum

of PACs of two constituents (individual slabs) are obtained after removal of one or the other part without optimizations.

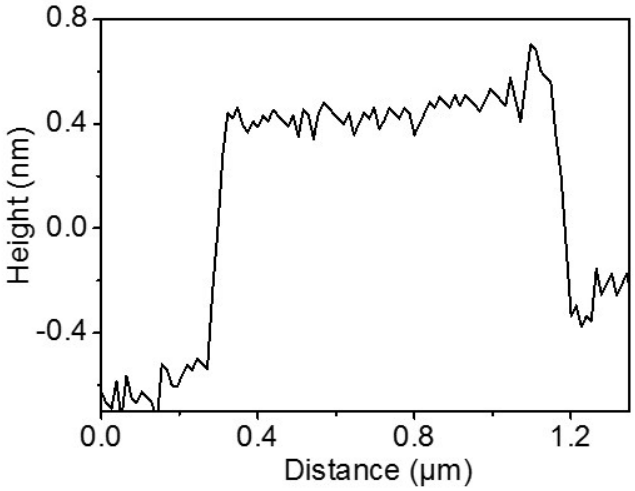

Figure S1 AFM Height line profiles

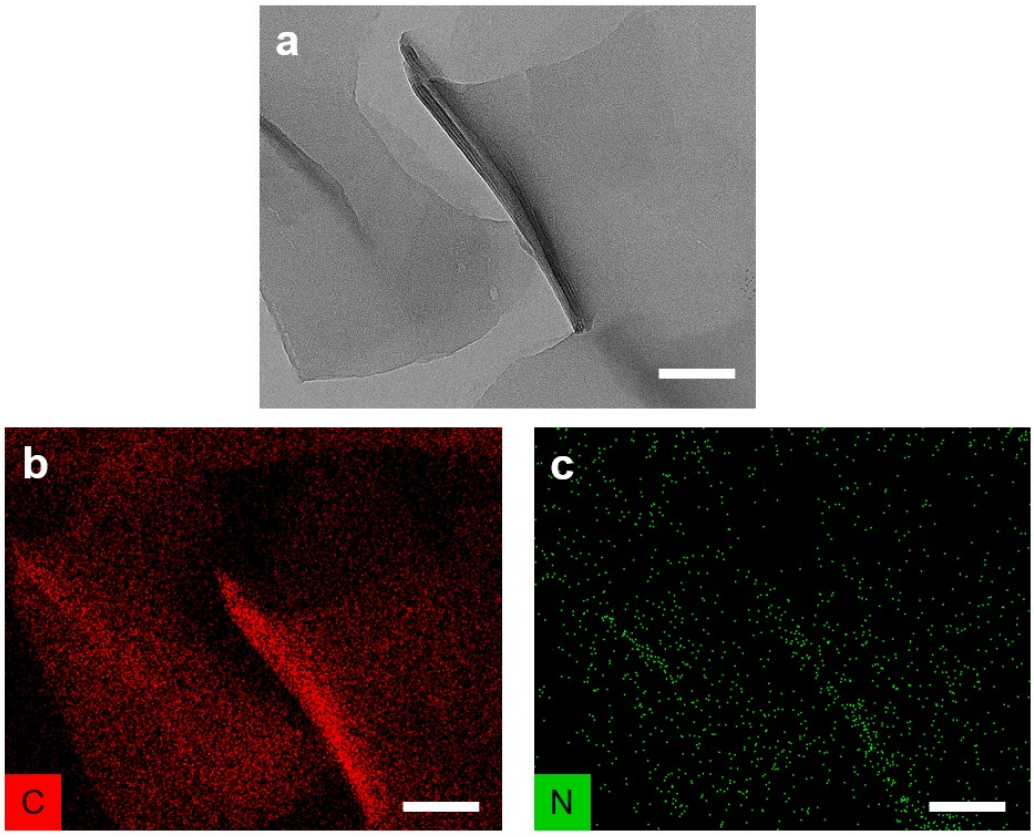

Figure S2 G-NH_2: (a) bright-field TEM image, (b) C elemental map, and (c) N elemental map. Scale bar = 100 nm.

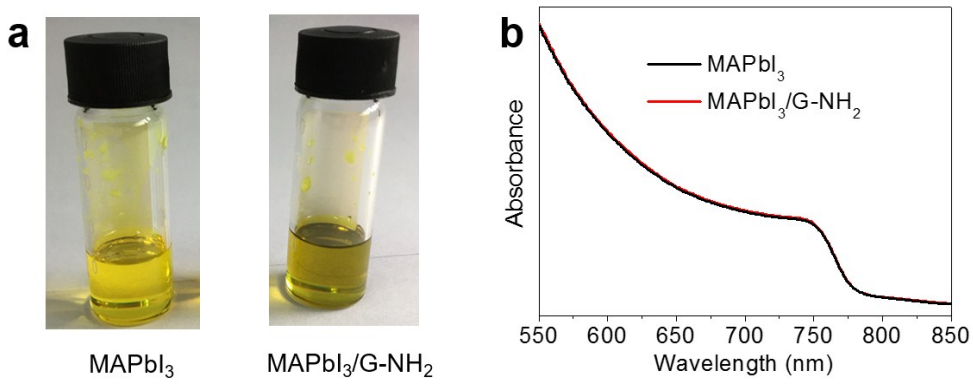

Figure S3 (a) Photographs of the $MAPbI_3$ precursor solutions with and without the optimal G-NH_2 addition, (b) corresponding UV-vis spectra from the fabricated films

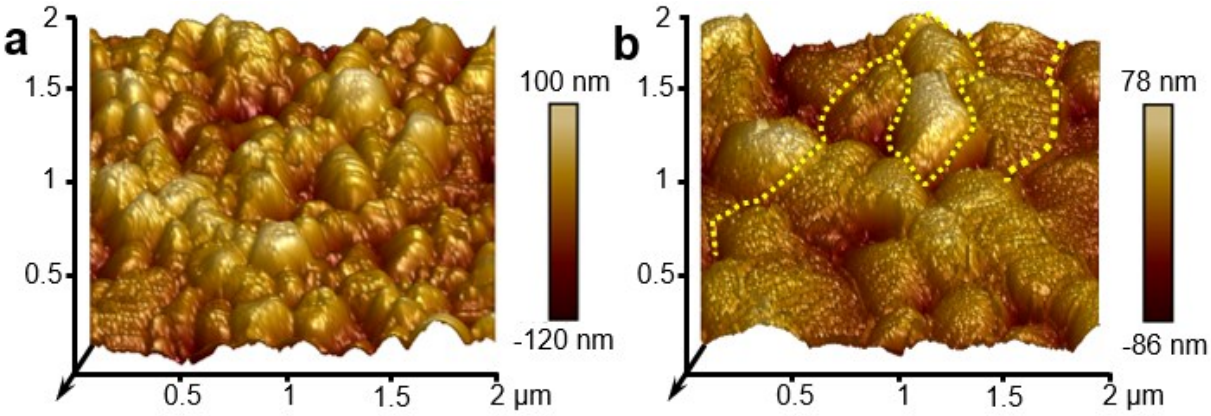

Figure S4 AFM images of thin films: (a) $MAPbI_3$ and (b) $MAPbI_3$/G-NH_2.

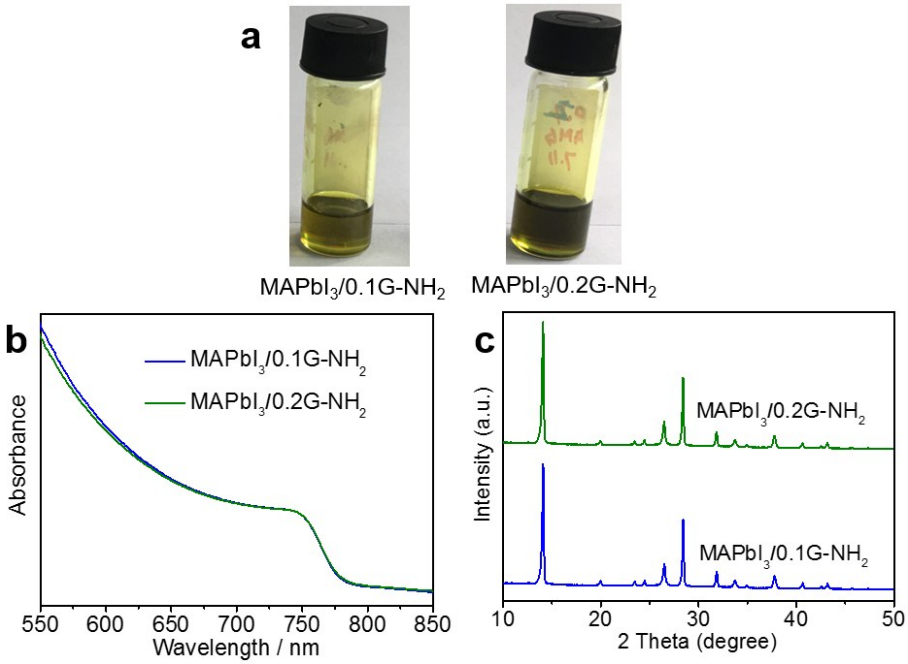

Figure S5 (a) Photographs of the $MAPbI_3$ precursor solutions with increasing G-NH_2 contents. Corresponding fabricated thin films: (b) UV-vis spectra and (c) XRD patterns.

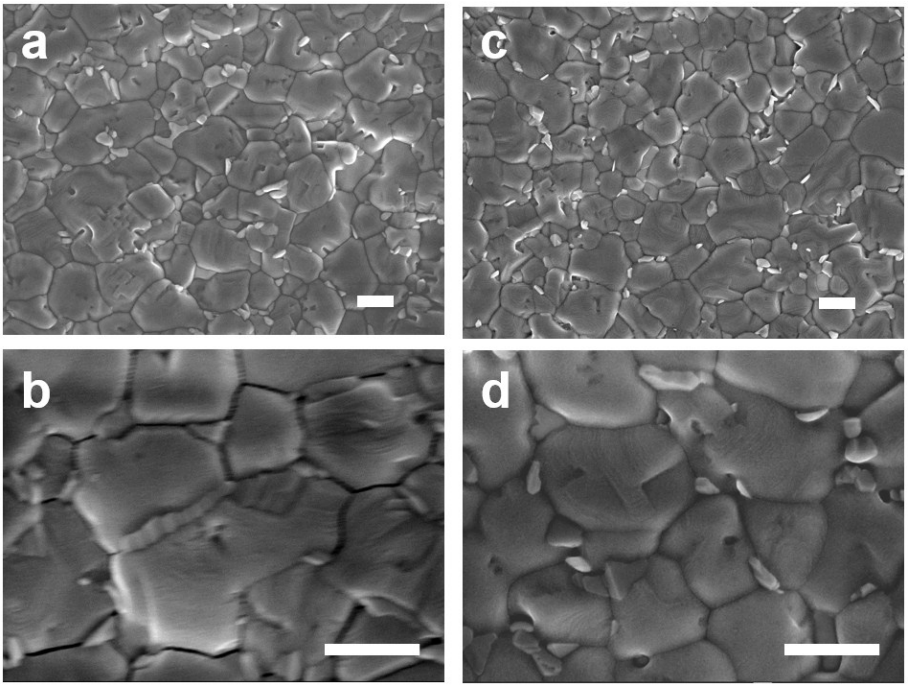

Figure S6 Top-surface images of the perovskite films with different G-NH_2 contents: (a)-(b) $MAPbI_3$/0.1G-NH_2, (c)-(d) $MAPbI_3$/0.2G-NH_2. Scale bars = 500 nm.

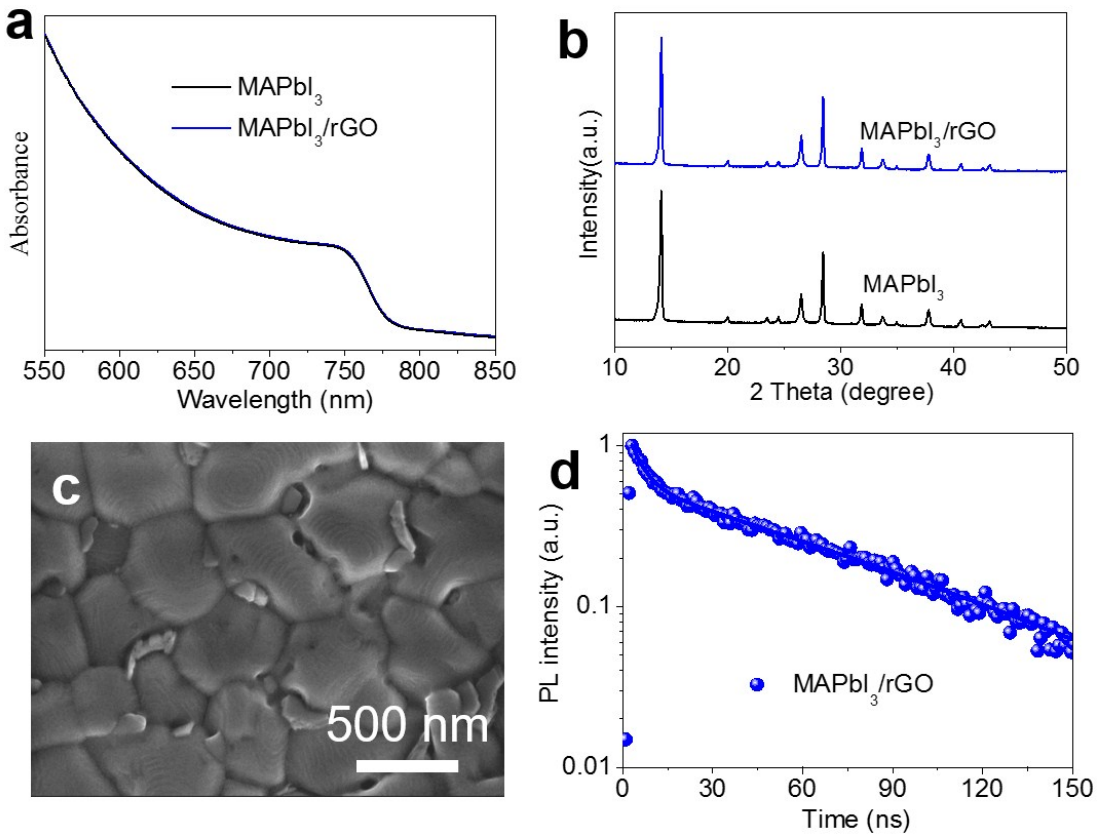

Figure S7 (a) UV-vis spectra and (b) XRD patterns of $MAPbI_3$ and $MAPbI_3$/rGO thin films. (c) Top-surface SEM image of the $MAPbI_3$/rGO film, (d) TRPL decay curves of $MAPbI_3$/rGO thin films. The measurements were performed from the perovskite film side.

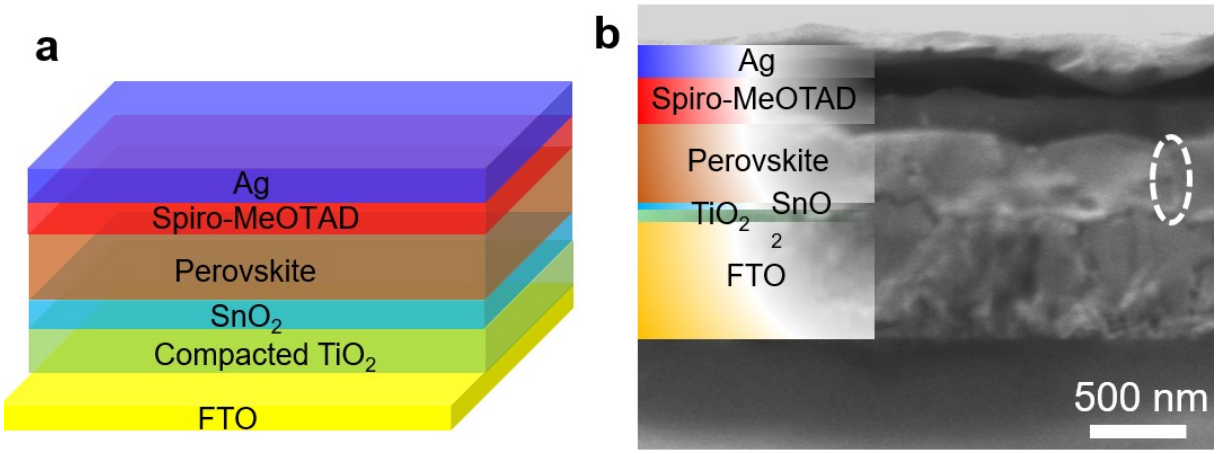

Figure S8 (a) Schematic illustration of the PSC device structure. (b) Cross-sectional SEM image of the $MAPbI_3$/G-NH_2-based PSC device. The dashed oval indicates a grain boundary.

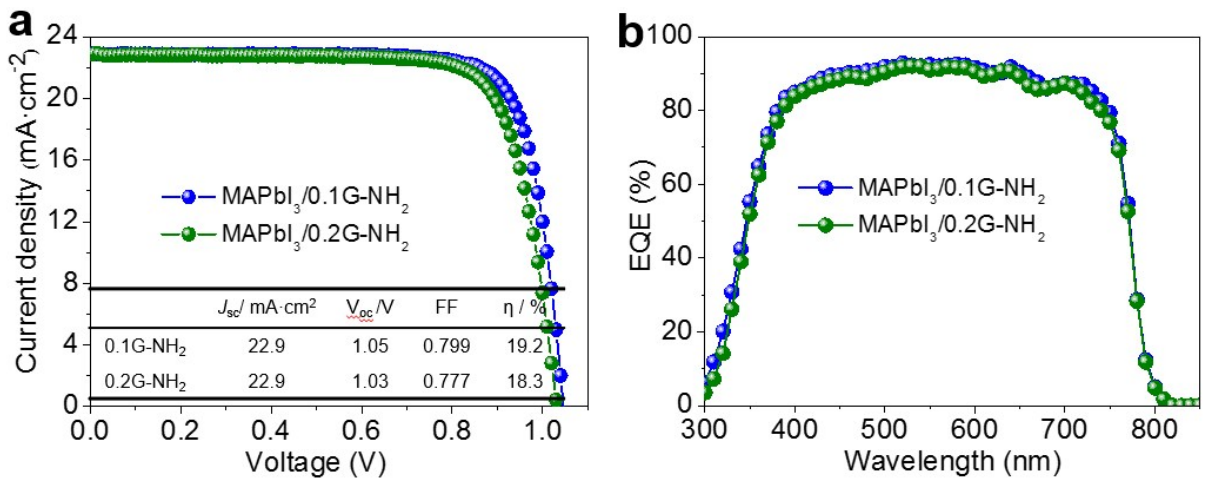

Figure S9 (a) J-V curves of PSCs based on $MAPbI_3$ (with different G-NH_2 contents) in reverse scan. (b) The corresponding EQE spectrum of the champion PSCs.

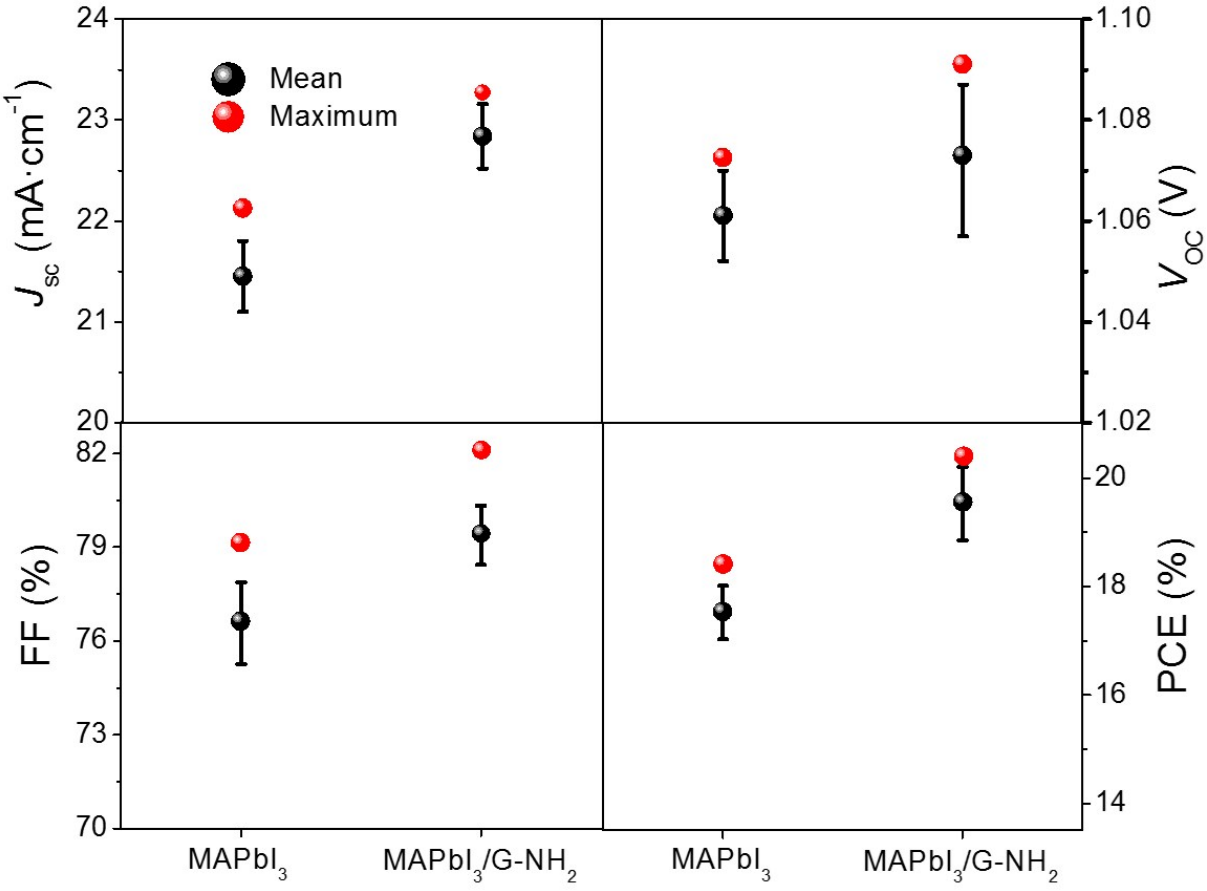

Figure S10 Detailed statistics of the PV parameters of PSCs based on $MAPbI_3$ without and with G-NH_2 (0.1 cm^2 effective cell area).

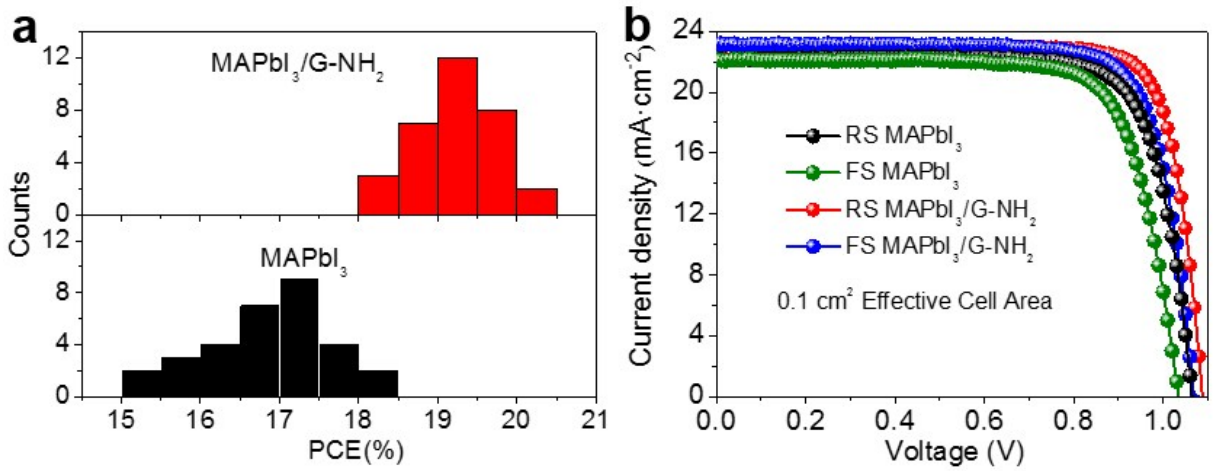

Figure S11 Champion PSCs characterization (0.1 cm^2 effective cell area). (a) PV performance statistics, (b) J-V characteristics of PSCs based on $MAPbI_3$ with and without G-NH_2 under simulated AM 1.5G solar illumination of 100 $mW \cdot cm^{-2}$.

Table S1 PV parameters of 'champion' PSCs based on $MAPbI_3$ without and with G-NH_2 (0.1 cm^2 effective cell area).

	Scan	J_{sc}/mA·cm^{-2}	V_{oc}/V	FF	PCE/%
$MAPbI_3$/G-NH_2	Reverse	23.1	1.09	0.815	20.4
	Forward	23.1	1.07	0.785	19.4
$MAPbI_3$	Reverse	22.1	1.07	0.787	18.5
	Forward	22.1	1.04	0.746	17.1

Table S2 Average PV parameters of large-area PSCs based on $MAPbI_3$ without and with G-NH_2 (1 cm^2 effective cell area; 22 devices).

	J_{sc}/mA·cm^{-2}	V_{oc}/V	FF	PCE/%
$MAPbI_3$/G-NH_2	22.1±0.4	1.09±0.02	0.714±0.023	17.4±0.7
$MAPbI_3$	20.4±0.1	1.06+0.02	0.609±0.025	13.2±0.5

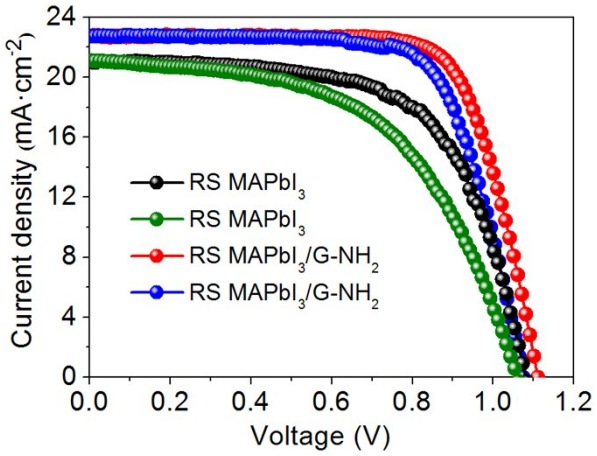

Figure S12 J-V curves for PSCs based on $MAPbI_3$ without and with G-NH_2 (1 cm^2 effective cell area) under a simulated AM 1.5G solar illumination of 100 $mW \cdot cm^{-2}$.

Table S3 PV parameters of large-area 'champion' PSCs based on $MAPbI_3$ without and with G-NH_2 (1 cm^2 effective cell area).

	Scan	J_{sc}/$mA \cdot cm^{-2}$	V_{oc}/V	FF/	PCE/%
$MAPbI_3$/G-NH_2	Reverse	22.8	1.11	0.739	18.7
	Forward	22.8	1.07	0.709	17.3
$MAPbI_3$	Reverse	21.1	1.08	0.632	14.4
	Forward	21.1	1.06	0.540	12.1

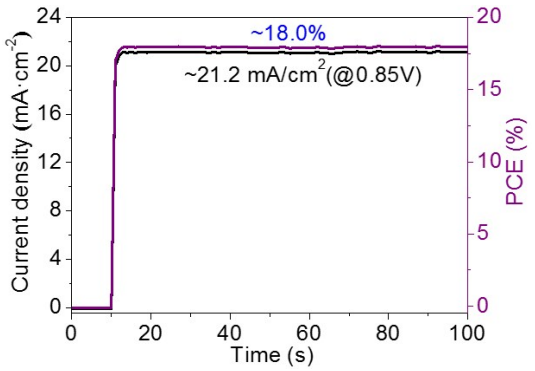

Figure S13 PCE and J output at a maximum power point of 0.85 V for the $MAPbI_3$/G-NH_2-based 'champion' PSC.

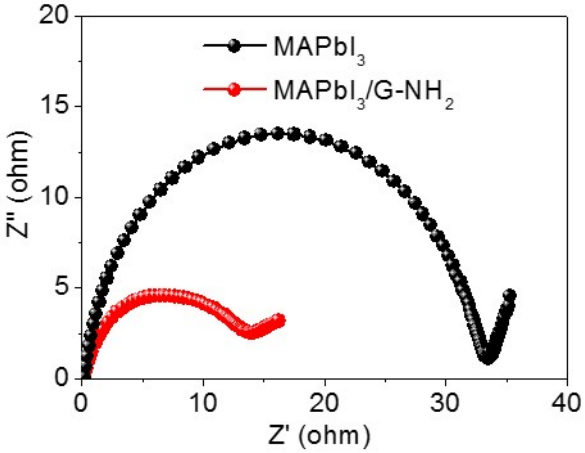

Figure S14 EIS characteristics of PSCs based on $MAPbI_3$ with and without G-NH_2 under illumination.

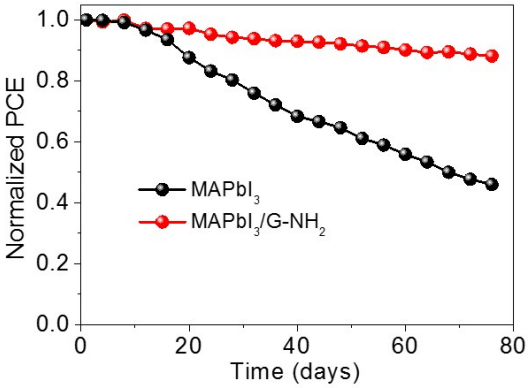

Figure S15 PCE of the 'champion' PSC based on $MAPbI_3$ without and with G-NH_2 as a function of storage time in a dark box at 20–30% RH and 25–30 °C.

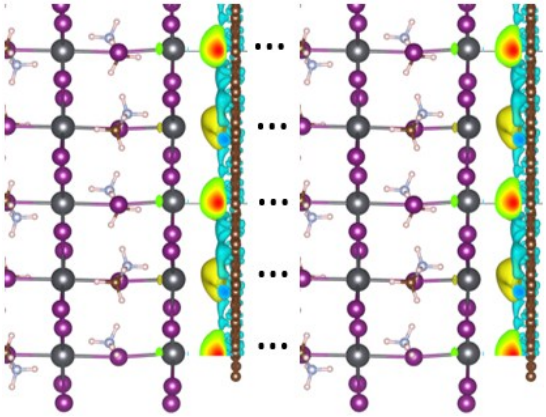

Figure S16 Calculated charge density at interfaces of $MAPbI_3$ with rGO (yellow=positive, cyan=negative).

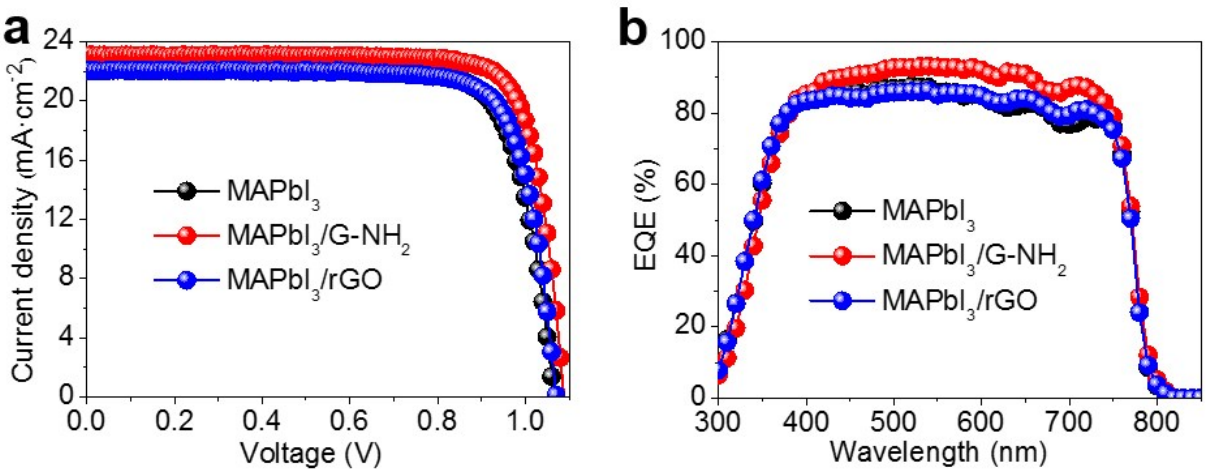

Figure S17 J-V curves for PSCs based on $MAPbI_3$, $MAPbI_3$/G-NH_2 and $MAPbI_3$/rGO (0.1 cm^2 effective cell area). (b) Corresponding EQE spectrum of the 'champion' PSC.

Reference

(1) Zhang, C.; Hao, R.; Liao, H.; Hou, Y., *Nano Energy* 2013, **1**, 88-97.

(2) Zhao, Y.; Zhu, K.. *J. Phys. Chem. C*, 2014, **18**, 9412-9418.